

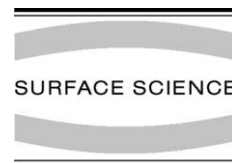


ELSEVIER

Available online at [www.sciencedirect.com](http://www.sciencedirect.com)

SCIENCE @ DIRECT®

Surface Science 530 (2003) 87–100



[www.elsevier.com/locate/susc](http://www.elsevier.com/locate/susc)

# Structure and stability of Fe<sub>3</sub>C-cementite surfaces from first principles

Wun C. Chiou Jr., Emily A. Carter \*

*Department of Chemistry and Biochemistry, University of California, Box 951569, Los Angeles, CA 90095-1569, USA*

Received 27 September 2002; accepted for publication 19 February 2003

## Abstract

We report results of gradient-corrected pseudopotential-based density functional theory calculations on bulk Fe<sub>3</sub>C in the cementite structure and its (001), (110), (011), (100), (101), (010), and (111) surfaces. Bulk properties are in reasonable agreement with available experimental data. The cementite local density of states shows predominantly metallic character, along with some polar covalent bonding contributions (charge transfer from iron to carbon) for both bulk and surfaces. We predict cementite surface energies in the range of 2.0–2.5 J/m<sup>2</sup>, most of which are lower than all pure Fe surface energies. In particular, we predict the Fe<sub>3</sub>C (001) surface to be the most stable and the Fe<sub>3</sub>C (100) surface to be the least stable. We show that greater stability is associated with localized Fe–C bonding at the surface, smoother surfaces created, e.g., by large C atom relaxation into the bulk, and more uniform coordination at the surface. The relatively greater stability of Fe<sub>3</sub>C surfaces is suggested to provide the driving force for cementite to form at the surfaces of bcc iron. Implications for the carburization erosion mechanism for steel, such as cracking and melting, are discussed.

© 2003 Elsevier Science B.V. All rights reserved.

*Keywords:* Density functional calculations; Steel; Corrosion; Surface energy; Iron; Carbides

## 1. Introduction

Under certain circumstances, extended use damages and erodes exposed steel surfaces. The harsh operating environments responsible for this effect may include high pressures, ultrahigh (e.g., 1700 K) temperatures, reactive gas mixtures (such as H<sub>2</sub>, O<sub>2</sub>, CO, CO<sub>2</sub>, NO, and NO<sub>2</sub>), and intense mechanical shock forces [1,2]. Although protective

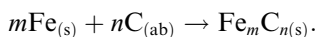
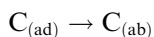
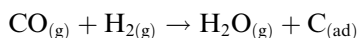
coatings, such as chromium, typically cover the steel surface [2,3], the smallest crack or failure in that coating exposes the vulnerable steel below it to erosion by many potential mechanisms. The mostly-iron steel may undergo oxidation, hydrogen embrittlement, sulfurization, carburization, and melting [4–6]. These processes may contribute to spallation of the coating to exacerbate the erosion. Fatigue and erosion of the steel limits the operational lifetime of the steel component in terms of safety and effectiveness. In addition, both the deposition and subsequent erosion of chromium coatings elicits environmental contamination and health concerns [7]. Within these harsh

\* Corresponding author. Tel.: +1-310-206-5118; fax: +1-310-267-0319.

E-mail address: [eac@chem.ucla.edu](mailto:eac@chem.ucla.edu) (E.A. Carter).

environments, in situ experiments are difficult, rendering it unclear as to which erosion mechanism dominates and to what degree.

The present work focuses on the product of one of the possible chemical mechanisms for steel erosion: carburization to produce the most stable carbide of iron,  $\text{Fe}_3\text{C}$  (cementite). This high-temperature reaction is caused by environmental carbon absorption into iron and steel surfaces, subsequently inducing precipitation of internal carbides and changes in mechanical properties [1]. Carburization begins with transport of atmospheric carbon, in one form or another, to the steel surface. The adsorbed carbon then diffuses into the surface and undergoes a solid state reaction with Fe in the steel when the carbon concentration is sufficiently high, as in:



The consequences of the changes brought about by carburization include stresses induced by volume changes from phase transformations, altered ductile properties and grain cohesion, and melting-point lowering [1]. The latter change is significant because the new melting point ( $T_M$ ) may fall below the typical operating temperature of the steel component,  $T_{M,\text{old}} \sim 1800 \text{ K} \rightarrow T_{M,\text{new}} < 1200 \text{ K}$ , leading to erosion by melting. Extreme cases of carburization may also lead to destructive metal dusting [8–10], the disintegration of iron, nickel,

and cobalt-based alloys into a metal-particle and carbon-particle dust:



Carburization-based erosion affects many industries [1], including: petrochemicals, steam reforming, industrial furnaces,  $\text{CO}_2$ -cooled nuclear reactors, coal gasification processes, and military applications [2].

Although steel typically contains a very small amount of carbon (for hardness), excess carbon ingress from the environment eventually leads to saturation. At temperatures below about 1000 K and C content below about 25%, the iron–carbon phase diagram primarily consists of  $\alpha$ -Fe (body-centered cubic, bcc) and cementite,  $\text{Fe}_3\text{C}$  [11,12]. Hence, in this range the most stable saturated carbide of iron is  $\text{Fe}_3\text{C}$  in the cementite structure, which is still metastable with respect to ground-state ( $\alpha$ ) iron and graphite. Its complicated structure consists of four formula units per orthorhombic unit cell, and has the space group *Pnma* (No. 62) [13–15], see Fig. 1 and Table 1. The unit cell contains eight iron atoms in “general” positions ( $8 \text{ Fe}_g$ ), four iron atoms in “special” positions ( $4 \text{ Fe}_s$ ), and four carbon atoms in the large interstices ( $4 \text{ C}$ ). The  $\text{Fe}_g$  are 14-coordinate, with 11 Fe–Fe bonds and 3 Fe–C bonds. The  $\text{Fe}_s$  are also 14-coordinate, but with 12 Fe–Fe bonds and 2 Fe–C bonds. The C are eight-coordinate and encased within six Fe atoms in a triangular prism structure, with two other Fe atoms slightly further out.  $\text{Fe}_s$  has a 0.05 Å greater mean radius than  $\text{Fe}_g$ , resulting in interatomic Fe–Fe

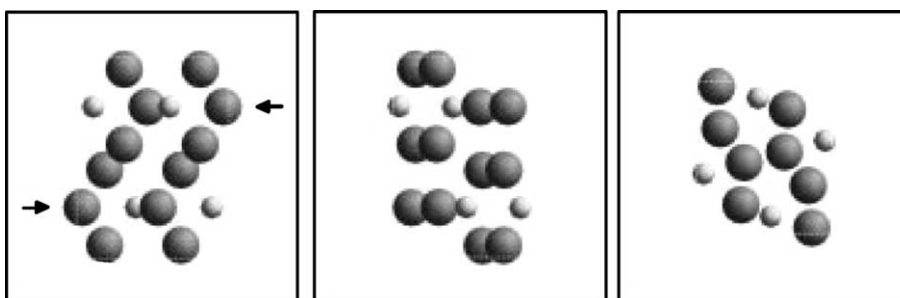


Fig. 1. Three views of the cementite bulk unit cell. The atoms are shown as spheres, light gray for C and dark gray for Fe. Shown from left to right are the top views of the (001), (100), and (010) viewplanes, respectively. The arrows in the (001) view identify two of the four Fe in special positions. The other two also occur at the vertices of the zig-zag planes formed by Fe in this perspective.

Table 1  
The cementite primitive unit cell structure in lattice coordinates

| Atom            | Basis vectors ( $a_0\mathbf{x}, b_0\mathbf{y}, c_0\mathbf{z}$ )   |
|-----------------|---|
| C               | $(+x_1, +\frac{1}{4}, +z_1), (-x_1, +\frac{3}{4}, -z_1), (\frac{1}{2} - x_1, +\frac{3}{4}, \frac{1}{2} + z_1), (\frac{1}{2} + x_1, +\frac{1}{4}, \frac{1}{2} - z_1)$  |
| Fe <sub>s</sub> | $(+x_2, +\frac{1}{4}, +z_2), (-x_2, +\frac{3}{4}, -z_2), (\frac{1}{2} - x_2, +\frac{3}{4}, \frac{1}{2} + z_2), (\frac{1}{2} + x_2, +\frac{1}{4}, \frac{1}{2} - z_2)$  |
| Fe <sub>g</sub> | $(+x_3, +y_3, +z_3), (-x_3, -y_3, -z_3), (\frac{1}{2} + x_3, \frac{1}{2} - y_3, \frac{1}{2} - z_3), (\frac{1}{2} - x_3, \frac{1}{2} + y_3, \frac{1}{2} + z_3), (-x_3, \frac{1}{2} + y_3, -z_3),$<br>$(+x_3, \frac{1}{2} - y_3, +z_3), (\frac{1}{2} - x_3, -y_3, \frac{1}{2} + z_3), (\frac{1}{2} + x_3, +y_3, \frac{1}{2} - z_3)$ |

The unit cell is scaled by the lattice constants ( $a_0, b_0, c_0$ ). The listed basis vectors determine the lattice positions of each of the four C atoms, four Fe<sub>s</sub> atoms, and eight Fe<sub>g</sub> atoms, as they depend on the parameters  $x_i, y_i$ , and  $z_i$ , numbers on [0,1].

distances  $d(\text{Fe}_s - \text{Fe}_s) > d(\text{Fe}_s - \text{Fe}_g) > d(\text{Fe}_g - \text{Fe}_g)$ . However, the Fe–C interatomic distances are greater for Fe<sub>g</sub> than Fe<sub>s</sub>:  $d(\text{Fe}_g - \text{C}) > d(\text{Fe}_s - \text{C})$  [14]. The bulk material is metallic and ferromagnetic. Although the structure is difficult to visualize, one may roughly consider the structure to be a series of zig-zag folded hexagonal close-packed (hcp) basal planes of Fe, with C occupying the interstitial regions at the fold vertices [16].

Although cementite presence within steel has been studied in detail, the difficulty in preparing bulk single-phase samples of Fe<sub>3</sub>C-cementite has resulted in a dearth of experimental data for many of its physical properties. Nevertheless, various samples of cementite have been characterized. The Fe–C system has been studied to evaluate the formation of various carbides and carbon segregation [17–19], and cementite particles or films have been prepared in various ways [20–22]. Some properties of bulk cementite have been measured, e.g. the Young's modulus of cementite films [22,23], the bulk modulus of polycrystalline cementite [24], the cementite lattice parameter temperature dependence in an Fe–C matrix [25], and the core electron binding energies of cementite components using X-ray photoelectron spectroscopy [26–28]. For cementite surfaces, Inokuti examined cementite formation on Fe, proposing a  $[002]_{\text{cementite}}//[011]_{\text{Fe}}$  interface [29], while Ohmori et al. found several other possible orientation relationships [30]. In general, however, the literature lacks accurate experimental data on well-defined single-phase, single-crystal cementite and its surfaces.

Thus, researchers have undertaken a few theoretical investigations on the Fe–C system and cementite. Wu, Freeman, and Olson used full-potential linear augmented plane-wave density

functional theory (DFT) with the local density approximation (LDA) to identify carbon as a solute which increases the cohesion of Fe grain boundaries [31]. Bulk cementite has been studied by Häglund et al. [32] as well as Vakhnej et al. [33] using all-electron linear muffin-tin orbital (LMTO) LDA band structure calculations. To our knowledge, however, there are no published theoretical investigations on the surfaces of Fe<sub>3</sub>C-cementite.

In this work, we present DFT predictions for several physical properties of Fe<sub>3</sub>C (cementite) bulk crystal and its low-index surfaces, as a first step toward understanding the carburization mechanism for steel erosion. Section 2 provides information on the theoretical methods employed. Section 3 presents results and analysis. Finally, Section 4 summarizes our findings and their implications.

## 2. Computational details

We carried out spin-polarized DFT [34,35] calculations within the Vienna Ab initio Simulation Package (VASP), version 4.4 [36–38]. The Kohn–Sham DFT equations are solved using a plane-wave basis set and periodic boundary conditions. Ultrasoft pseudopotentials (USPP) based upon those first proposed by Vanderbilt [39,40] are used to represent the effect of the nuclei plus core electrons on the valence electrons. Electron exchange and correlation is approximated using the Perdew and Wang PW91 [41,42] formulation of the generalized gradient approximation (GGA) for the exchange-correlation functional. GGA is used instead of the LDA, because LDA predicts the incorrect ground state for bulk iron [43], while GGA correctly determines a ferromagnetic bcc ground

state. Utilizing the USPP's allows a lower kinetic energy cutoff (i.e., a smaller plane-wave basis set) than norm-conserving pseudopotentials of the same quality, and these USPP's have been shown to yield fairly accurate results for bulk magnetic systems like iron [44].

We used the standard pseudopotentials supplied with VASP package, which have been made with the RRKJ scheme [45]. The USPP for carbon was generated in the non-magnetic  $2s^2 2p^2$  configuration, with no partial (non-linear) core correction to electron exchange and correlation. The local part of this potential corresponds to the d pseudopotential linearly unscreened with respect to the valence electrons. The C pseudopotential core outer pseudization cutoff radius was 0.96 Å, and was augmented with two s and p projectors and one d. The ultrasoft s and p channels included a cutoff radius of 0.70 Å for the augmentation part along with 0.86 and 0.96 Å cutoffs, respectively, for the non-norm-conserving part. The d channel was norm-conserving with a cutoff radius of 0.96 Å. The USPP used for iron was generated in the non-magnetic  $4s^1 3d^7$  configuration. The local part of this potential is a non-linearly unscreened all-electron potential, with a cutoff radius of 0.90 Å. The Fe pseudopotential outermost pseudization radius was 1.30 Å, and it was augmented with two projectors each for s, p, and d. The s channel was norm-conserving with a radial cutoff of 1.16 Å. The ultrasoft p and d channels included cutoff radii of 1.16 and 1.05 Å, respectively, for their augmentation part, and a common cutoff of 1.30 Å for their non-norm-conserving part. This Fe potential also employed a 0.51 Å non-linear partial core correction cutoff.

For a metallic system like cementite, proper selection of a partial band occupation method not only helps with convergence efficiency, but is essential for reaching the correct total energy. We used a combination of two such methods to assist each single-point calculation. First, a calculation was done using the Methfessel–Paxton (MP) Fermi surface smearing method [46] with a 0.15 eV smearing width. The converged Kohn–Sham orbitals from this step were then used as an initial guess for a second calculation in which we switched to the tetrahedron occupation method with Blöchl cor-

rections [47]. We employed this two-step procedure both to assist convergence to the global energy minimum and to limit “charge sloshing”, which can pose a problem in metals. For both steps, a residual minimization method—direct inversion in the iterative subspace (RMM-DIIS) [38,48–50] was used to further enhance convergence of the Kohn–Sham equations.

The total energy was then converged with respect to both kinetic energy cutoff and  $k$ -point sampling for both bulk and surface unit cells. Following this, a conjugate gradient (CG) algorithm [38,51] relaxed the ions and cell shape, and a final set of static calculations utilizing the converged parameters and structure was carried out. Only the MP smearing method was used during ionic relaxation, while the two-step smearing/tetrahedron method described above was used for the final static calculation. The stopping criterion for electronic self-consistent interactions was convergence of the total energy to within  $10^{-4}$  eV, and the stopping criterion for ionic relaxations was convergence of the total energy to within  $10^{-3}$  eV of the previous ionic step.

For the bulk calculations, we found it necessary to employ (for full convergence) a  $9 \times 6 \times 10$   $k$ -point Monkhorst–Pack grid, which corresponds to a  $k$ -point spacing between 0.022 and 0.025 Å<sup>-1</sup> and 75 irreducible  $k$ -points. Convergence of the basis set required a 400 eV kinetic energy cutoff for the pseudocharge and a 679 eV kinetic energy cutoff for the augmentation charge. The smearing width was also varied, and we found 0.15 eV smearing was sufficient to limit the entropy to less than 1 meV/atom. The experimental structure [14] was taken as the initial bulk model, which was then allowed to relax as described above to find the minimum energy structure.

We selected seven surface cuts from the relaxed bulk structure for analysis: (1 0 0), (0 0 1), (1 1 0), (0 1 1), (1 0 1), (0 1 0), and (1 1 1). Specific cuts were chosen to maintain surface stoichiometry as much as possible, as well as to ensure inversion symmetry at the center of the slab. For the case of cementite, this required slabs corresponding to integer multiples of the bulk unit cell thickness. Although half-integer multiple cementite slabs maintain equivalent faces, they lose inversion symmetry and

produced anomalous surface energies in our convergence calculations. We considered two figures of merit to determine if our parameters (slab and vacuum thickness, kinetic energy cutoff, and  $k$ -point sampling) were converged for modeling a surface: we required the density of states (DOS) of the inner layers of each slab to look bulk-like, and we required that the bulk-terminated surface energies be converged.

Convergence with thickness of the slab was analyzed by comparing the inner-layer DOS for the unrelaxed slab to the bulk crystal DOS (see Fig. 2). When they become similar, the slab thickness should be sufficient such that each surface experi-

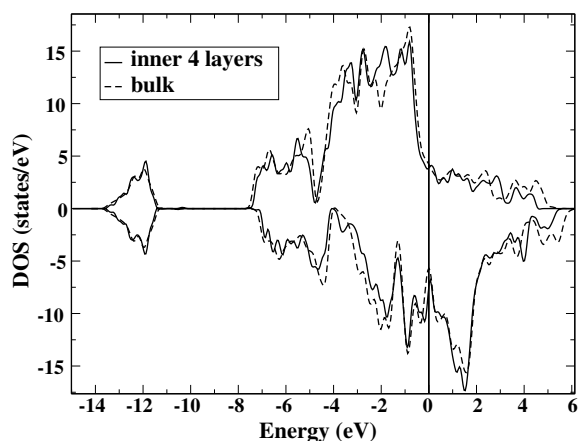


Fig. 2. Convergence of the inner-layer DOS for (001) cementite surface to the total DOS of the cementite bulk. The plot shows the up (>0) and down (<0) spin DOS components of the inner four layers of a 12-layer slab.

ences an electronic environment as if it is connected to an infinite bulk crystal. Vacuum thickness was set equal to slab thickness for these layer convergence tests, and values of kinetic energy cutoff and  $k$ -point spacing similar to those required for bulk convergence were employed. Then, once a suitable number of layers was found (according to the DOS), we performed an additional calculation with a higher kinetic energy cutoff and more  $k$ -points to verify that the parameters used in the previous step were sufficient. Finally, we checked whether our chosen vacuum layer was sufficiently thick by reducing it for thinner slabs and checking the resulting surface energies. The convergence behaviors for the energies of the (100) surface and the (001) surface are shown in Table 2.

All unrelaxed surfaces had converged surface energies at about 400 eV for the pseudocharge kinetic energy cutoff (the same  $E_{\text{cut}}$  for the augmentation charge as used for bulk  $\text{Fe}_3\text{C}$  was employed for surfaces), similar  $k$ -point spacing to the bulk cell, and stoichiometric layers corresponding to three bulk unit cells (one bulk cell is four  $\text{Fe}_3\text{C}$  layers for (001) and (100) surfaces and two  $\text{Fe}_6\text{C}_2$  layers for the other surfaces; see Table 5 presented later), for a total of 48 atoms in each slab unit cell. Larger surface unit cells were not considered due to the expense; we therefore could not assess if any long-range reconstructions of the surfaces would be favorable. Vacuum thickness equaling the converged slab thickness was also found to be sufficient for all surfaces. For example, for the (001) surface, 12 stoichiometric layers, 13.5 Å of

Table 2

Convergence of the energy ( $E_{\text{surf}}$ ) of the unrelaxed  $\text{Fe}_3\text{C}$  (100) and (001) surfaces: number of layers of  $\text{Fe}_3\text{C}$  stoichiometric units, vacuum thickness, plane wave kinetic energy cutoff ( $E_{\text{cut}}$ ), and surface Brillouin zone irreducible  $k$ -point sampling

| Surface | No. of layers | Vacuum (Å) | $E_{\text{cut}}$ (eV) | Irreducible $k$ -pts (mesh) | $E_{\text{surf}}$ (J/m <sup>2</sup> ) |
|---------|---------------|------------|-----------------------|-----------------------------|---------------------------------------|
| (100)   | 8             | 10.27      | 400                   | 15 (10 × 6 × 1)             | 3.143                                 |
| (100)   | 8             | 15.20      | 400                   | 15 (10 × 6 × 1)             | 2.938                                 |
| (100)   | 12            | 15.20      | 400                   | 15 (10 × 6 × 1)             | 2.716                                 |
| (100)   | 12            | 15.20      | 450                   | 24 (12 × 8 × 1)             | 2.712                                 |
| (001)   | 8             | 9.02       | 400                   | 12 (8 × 6 × 1)              | 2.433                                 |
| (001)   | 8             | 13.54      | 400                   | 12 (8 × 6 × 1)              | 2.585                                 |
| (001)   | 12            | 13.54      | 400                   | 12 (8 × 6 × 1)              | 2.399                                 |
| (001)   | 12            | 13.54      | 450                   | 24 (11 × 8 × 1)             | 2.395                                 |

Table 3  
Converged parameters used for the calculations of the surfaces discussed

| Surface | No. of layers | Vacuum (Å) | $E_{\text{cut}}$ (eV) | Irreducible $k$ -pts, (mesh), spacing (Å <sup>-1</sup> ) |
|---------|---------------|------------|-----------------------|--|
| (100)   | 12            | 15.2       | 400                   | 15, (10 × 6 × 1), 0.023                                  |
| (011)   | 6             | 11.3       | 400                   | 12, (1 × 8 × 5), 0.025                                   |
| (010)   | 6             | 16.9       | 400                   | 25, (1 × 10 × 9), 0.022                                  |
| (101)   | 6             | 10.1       | 400                   | 16, (7 × 7 × 1), 0.021                                   |
| (111)   | 6             | 9.0        | 400                   | 12, (6 × 7 × 1), 0.022                                   |
| (110)   | 6             | 12.2       | 400                   | 23, (9 × 5 × 1), 0.024                                   |
| (001)   | 12            | 13.5       | 400                   | 12, (8 × 6 × 1), 0.025                                   |

All surface slabs contained 48 atoms in the unit cell (either 12 Fe<sub>3</sub>C layers or 6 Fe<sub>6</sub>C<sub>2</sub> layers).

vacuum,  $E_{\text{cut}} = 400$  eV, and 12 irreducible  $k$ -points, were sufficient for a reasonable surface energy convergence. The final parameters used for the calculations in our analysis are presented in Table 3.

With these converged values of slab thickness, vacuum thickness, and  $k$ -point sampling, ionic relaxation using the optimized bulk lattice parameters proceeded via a CG algorithm with Fermi-surface smearing using a 30% lower kinetic energy cutoff than required for convergence. In addition, the inner half of each slab was kept fixed to lessen the computational effort. If the force on any ion within the slab exceeded 0.05 eV/Å, the fixed-atom restriction was removed and the ions were further relaxed to convergence. Single-point calculations using the converged plane-wave basis were then performed with the two-step smearing/tetrahedron occupation procedure on the optimized structures in order to evaluate the total energies.

Local density of states (LDOS) analysis provides a qualitative evaluation of charge transfer, covalent bonding/hybridization, and local magnetic moments. For this, the total DOS is projected onto spherical harmonics centered upon the atoms in the cell to estimate the local angular momentum contributions. The sphere radii selections can vary between just-touching and volume-filling choices. In the former, charge captured within the spheres is underestimated with respect to the full system charge, whereas in the latter several adjacent spheres may overlap and overestimate the total charge. For our analysis, we selected volume-filling radii of 1.23 and 1.35 Å for C

and Fe, respectively, in order to capture the maximum interstitial charge in this metallic system.

### 3. Results and analysis

#### 3.1. Bulk cementite

We compared our USPP-GGA results for bulk Fe<sub>3</sub>C in the cementite structure to those of Häglund et al. [52] (LMTO-LDA) and to experimental values. The semi-relativistic LMTO-LDA calculations employed a 64  $k$ -point mesh, the experimental structure, and similar Wigner–Seitz radii for the atomic spheres that we used for our projected DOS analysis. For the experimental data, lattice parameters are from X-ray diffraction [14], the cohesive energy is an estimate given in [52], and the magnetic moment is an average over all Fe atoms [26,27]. The results comparison is presented in Table 4.

The USPP DFT-GGA lattice constants deviate less than 1% from experiment. We therefore expect our structural predictions for surfaces should be quite accurate. The cohesive energy is calculated from

$$E_{\text{coh}} = \frac{1}{N_{\text{Fe}} + N_{\text{C}}} \left( \sum_{N_{\text{Fe}}} E_{\text{Fe}}^{\text{gs}} + \sum_{N_{\text{C}}} E_{\text{C}}^{\text{gs}} - E_{\text{bulk}} \right)$$

with  $N_{\text{Fe}} = 12$  iron atoms and  $N_{\text{C}} = 4$  carbon atoms in the cementite primitive unit cell. The VASP program reports cohesive energies ( $E_{\text{coh}}$ ) with respect to the atomic energies for the valence electron configuration used to generate the USPP

Table 4  
Bulk Fe<sub>3</sub>C properties

| Property  | USPP-GGA              | LMTO-LDA | Experiment            |
|---|-----------------------|----------|-----------------------|
| ( <i>a</i> <sub>0</sub> , <i>b</i> <sub>0</sub> , <i>c</i> <sub>0</sub> ) (Å) | (5.06, 6.74, 4.51)    |          | (5.09, 6.74, 4.53)    |
| ( <i>x</i> <sub>1</sub> , <i>z</i> <sub>1</sub> )                             | (0.877, 0.440)        |          | (0.890, 0.450)        |
| ( <i>x</i> <sub>2</sub> , <i>z</i> <sub>2</sub> )                             | (0.038, 0.837)        |          | (0.036, 0.850)        |
| ( <i>x</i> <sub>3</sub> , <i>y</i> <sub>3</sub> , <i>z</i> <sub>3</sub> )     | (0.176, 0.068, 0.332) |          | (0.186, 0.063, 0.328) |
| <i>E</i> <sub>coh</sub> (eV/atom)   | 5.24                  | 8.38     | 5.05                  |
| <i>M</i> <sub>0</sub> (μ <sub>B</sub> /Fe <sub>g</sub> )                      | 1.95                  | 1.74     | (1.78)*               |
| <i>M</i> <sub>0</sub> (μ <sub>B</sub> /Fe <sub>s</sub> )                      | 1.99                  | 1.98     | (1.78)*               |
| <i>M</i> <sub>0</sub> (μ <sub>B</sub> /C)                                     | −0.16                 | −0.06    |                       |
| <i>B</i> <sub>0</sub> (GPa)   | 142                   |          | 174                   |

Comparison of pseudopotential GGA, all-electron LMTO-LDA, and experimental properties: lattice constants (*a*<sub>0</sub>, *b*<sub>0</sub>, *c*<sub>0</sub>), lattice parameters (*x*<sub>*i*</sub>, *y*<sub>*i*</sub>, *z*<sub>*i*</sub>), cohesive energy (*E*<sub>coh</sub>), magnetic moments per atom (*M*<sub>0</sub>), including Fe in general (g) and special (s) positions, and bulk modulus (*B*<sub>0</sub>).

\*Averaged value over all Fe.

[44,53]. For Fe and C, the GGA USPP's were constructed using non-magnetic 3d<sup>7</sup>4s<sup>1</sup> and 2s<sup>2</sup>2p<sup>2</sup> reference configurations, respectively, but the experimental ground states of Fe and C are high-spin 3d<sup>6</sup>4s<sup>2</sup> (<sup>5</sup>D) and 2s<sup>2</sup>2p<sup>2</sup> (<sup>3</sup>P), respectively. We therefore correct the VASP *E*<sub>coh</sub> and report it with respect to the USPP-GGA energies for the high-spin experimental ground states of the atoms. Not surprisingly, the GGA cohesive energy closely approaches the experimental estimate (differing by only about 4%), while the previous LMTO-LDA prediction grossly overestimates *E*<sub>coh</sub> due to the usual overbinding of the LDA. This gives us confidence that our USPP-GGA surface energy predictions will be reliable.

Magnetic moments were calculated from the site-projected DOS, taking the spin difference in the site-projected DOS integrated up to the Fermi level. These USPP DFT-GGA results generally agree well with the all-electron LDA calculations of Häglund et al., although the magnetic moment due to Fe<sub>g</sub> differs and raises the average *M*<sub>0</sub> to 1.97 μ<sub>B</sub>/Fe. This magnetic moment is a bit high compared to the experimental value.

We also performed several USPP-GGA single-point energy calculations [*E*(*V*)] with differing uniformly-scaled (from the relaxed equilibrium volume) cell volumes (*V*) and non-linearly fit these to the third-order Birch–Murnaghan [54,55] equation of state, *E*(*V*) = *E*<sub>1</sub> + *E*<sub>2</sub> + *E*<sub>3</sub>, where

$$E_1 = \frac{9}{4} B_0 V_0 \left( \frac{V_0}{V} \right) \left[ 0.5 \left( \frac{V_0}{V} \right)^{1/3} - \left( \frac{V}{V_0} \right)^{1/3} \right]$$

$$E_2 = \frac{9}{16} B_0 (B'_0 - 4) V_0 \left( \frac{V_0}{V} \right) \times \left[ \left( \frac{V_0}{V} \right) - 3 \left( \frac{V_0}{V} \right)^{1/3} + 3 \left( \frac{V}{V_0} \right)^{1/3} \right]$$

$$E_3 = E(V_0) - \frac{9}{16} B_0 V_0 (B'_0 - 6).$$

A best fit to these equations yields the bulk modulus *B*<sub>0</sub> = 142 GPa, its pressure derivative *B*'<sub>0</sub> = 4.60, and the equilibrium volume *V*<sub>0</sub> = 154.54 Å<sup>3</sup> (all at 0 K). These values are lower than recent experimental measurements, which yield *B*<sub>0</sub> = 174 GPa, *B*'<sub>0</sub> = 4.8, and *V*<sub>0</sub> = 155.28 Å<sup>3</sup> (all at 300 K). The differences in equilibrium volume are similar to experimental temperature-dependence estimates [25].

The bulk DOS and LDOS provide some insight into the bonding behavior within cementite. Fig. 3 compares the bulk Fe<sub>3</sub>C (cementite) total DOS to that of ground-state iron, α-Fe, while the bulk Fe<sub>3</sub>C site- and *l*-projected DOS are shown in Fig. 4. First of all, Fe<sub>3</sub>C has no band gap, and therefore exhibits metallic behavior as expected. Iron d-states dominate the Fe<sub>3</sub>C DOS near the Fermi level, similar to bulk iron, while carbon s and p contributions to the DOS are essentially zero at the Fermi level.

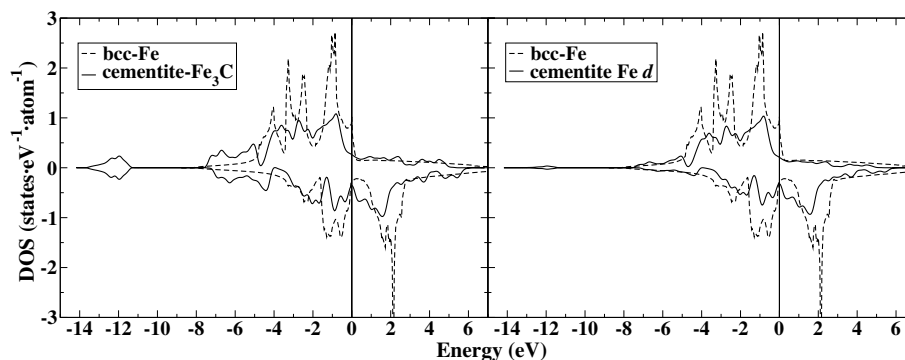


Fig. 3. Comparison of  $\alpha$ -Fe with  $\text{Fe}_3\text{C}$  bulk total DOS (left plot) and  $\text{Fe}_3\text{C}$  Fe-d-projected DOS (right plot). The “positive” and “negative” DOS are the up-spin and down-spin components, respectively. The vertical line is positioned at the Fermi level. Fe d states dominate the total DOS in  $\text{Fe}_3\text{C}$ .

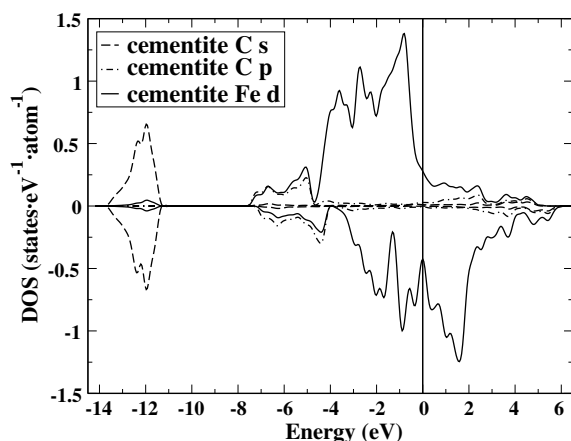


Fig. 4.  $\text{Fe}_3\text{C}$  bulk site- and  $l$ -projected DOS: C s, C p, and Fe d. The “positive” and “negative” DOS are the up-spin and down-spin components, respectively. The vertical line is positioned at the Fermi level.

The higher binding energy region 4–8 eV below the Fermi-level (Fig. 4) shows identically shaped features in the DOS from both Fe d and C p, suggesting a significant covalent bonding component between Fe and the interstitial C atoms in cementite. The corresponding Fe–C antibonding levels are evident, particularly around 2–4 eV above the Fermi level. Note also that the amplitude of the C peaks are nearly the same as the amplitude of the Fe d peaks here, despite the 3:1 element ratio favoring Fe. This is consistent with the integrated DOS charges suggesting that some charge transfer to carbon is occurring and the Fe–

C interaction is of a polar covalent nature. Integrated projected-DOS analysis qualitatively predicts only a small amount of charge transfer (total electrons/atom are 4.14 for C and 7.15 for Fe) from Fe to C within cementite compared to pure bulk Fe analyzed in the same manner (total electrons/atom for bcc Fe is 7.20). This polar covalent interaction between C and Fe proves to be important when bulk cementite is cleaved into different surfaces.

### 3.2. Surfaces

Examination of various bulk-terminated low-index  $\text{Fe}_3\text{C}$  surface cuts allows us to assess possible relative stabilities prior to carrying out DFT calculations. Stable surfaces are likely to exhibit minimal coordination changes (dangling bonds) for surface atoms, maintenance of surface stoichiometry, and high atom density. Table 5 shows our evaluation of the unrelaxed surfaces. In addition to the surface unit cell lattice vectors, it lists the number of dangling bonds per unit surface area as calculated by undercoordination relative to the bulk structure. Also given are the number of  $\text{Fe}_3\text{C}$  units per slab layer and the layer thickness from the outermost surface atom required to achieve such a stoichiometry. Referring to this table and the aforementioned criteria, one may expect surfaces such as (001), (010), and (101) to be stable due to their small stoichiometric layer thickness, high surface packing density, and min-

Table 5  
Analysis of Fe<sub>3</sub>C bulk-terminated surface structures

| Surface property                        | (100) | (011) | (010) | (101) | (111) | (110) | (001) |
|---|-------|-------|-------|-------|-------|-------|-------|
| $u$ (Å)                                 | 6.748 | 5.090 | 4.523 | 6.809 | 8.117 | 4.523 | 5.090 |
| $v$ (Å)                                 | 4.523 | 8.123 | 5.090 | 6.748 | 6.786 | 8.452 | 6.748 |
| Dangling bonds/Å <sup>2</sup>           | 0.72  | 0.82  | 0.78  | 0.70  | 0.78  | 0.73  | 0.76  |
| Stoichiometric layer thickness (Å)      | 0.699 | 1.174 | 2.459 | 1.236 | 1.181 | 1.148 | 0.485 |
| No. of Fe <sub>3</sub> C/layer          | 1     | 2     | 2     | 2     | 2     | 2     | 1     |
| Surface density (atoms/Å <sup>2</sup> ) | 0.131 | 0.193 | 0.347 | 0.174 | 0.145 | 0.209 | 0.116 |

( $u, v$ ) are the surface unit cell lattice vectors. These vectors are orthogonal for all surfaces except (111), where the angle is 111.7°.

imal density of dangling bonds, respectively. Alternatively, surfaces such as (001) and (011), might be expected to be less stable due to their low surface density and greater density of broken bonds, respectively.

Calculations were performed on the (001), (100), (011), (110), (101), (010), and (111) surfaces of cementite. The surface energy is given by

$$E_{\text{surf}} = (E_{\text{slab}} - NE_{\text{bulk}})/2A$$

where  $N$  is the number of Fe<sub>3</sub>C units in the slab,  $E_{\text{bulk}}$  is the bulk total energy per Fe<sub>3</sub>C unit,  $A$  is the surface area of the slab, and  $E_{\text{slab}}$  is the total energy for the slab.

We compared  $E_{\text{surf}}$  for each surface cut with its corresponding structural properties, both before and after relaxation, in order to predict possible stability correlations. Calculated properties for each surface (using converged parameters from Table 3) are shown in Table 6. In addition to the unrelaxed and relaxed surface energies, we also present several other properties. The relaxation

energy ( $E$ ) is the percent difference between the unrelaxed and relaxed surface energies. The root-mean-square relaxation (rms relax) is the difference in atomic positions before and after relaxation,

$$r_{\text{rms}} = \left[ \frac{1}{N} \sum_{i=1}^N (\mathbf{r}_{i0} - \mathbf{r}_i)^2 \right]^{1/2} \quad (1)$$

where  $\mathbf{r}_{i0}$  and  $\mathbf{r}_i$  are the unrelaxed and relaxed atomic position vectors for all 48 atoms in the slab, respectively. The rms relaxations normalized with respect to the surface areas of each surface unit cell are also presented. The final property shown, roughness, is calculated in a manner similar to Eq. (1), replacing the atomic position vectors  $\mathbf{r}_0$  and  $\mathbf{r}$  with only the surface-normal-direction component of the outer-layer (Fe<sub>3</sub>C or Fe<sub>6</sub>C<sub>2</sub>) atomic positions (e.g.  $z_{i,\text{avg}}$  and  $z_i$ ), and normalized to the layer thickness  $L$  instead of surface area to make it dimensionless:

$$r_{\text{rms}} = \frac{\left[ \frac{1}{N} \sum_{i=1}^N (z_{i,\text{avg}} - z_i)^2 \right]^{1/2}}{L} \quad (2)$$

Table 6  
USPP DFT-GGA Fe<sub>3</sub>C surface properties

| Surface property                                   | (100) | (011) | (010) | (101) | (111) | (110) | (001) |
|--|-------|-------|-------|-------|-------|-------|-------|
| $E_{\text{surf,unrel}}$ (J/m <sup>2</sup> )        | 2.72  | 2.58  | 2.40  | 2.40  | 2.45  | 2.37  | 2.40  |
| $E_{\text{surf,rel}}$ (J/m <sup>2</sup> )          | 2.47  | 2.37  | 2.26  | 2.25  | 2.22  | 2.19  | 2.05  |
| Relaxation $E$ (%)                                 | 9.2   | 8.1   | 5.8   | 6.3   | 9.4   | 7.6   | 14.6  |
| Rms relax (10 <sup>-3</sup> Å)                     | 84    | 109   | 63    | 95    | 147   | 106   | 108   |
| Rms relax/area (10 <sup>-3</sup> Å <sup>-1</sup> ) | 2.77  | 2.64  | 2.75  | 2.07  | 2.89  | 2.78  | 3.16  |
| Rms roughness (unrelaxed)                          | 0.30  | 0.29  | 0.26  | 0.30  | 0.30  | 0.25  | 0.27  |
| Rms roughness (relaxed)                            | 0.25  | 0.22  | 0.25  | 0.26  | 0.25  | 0.19  | 0.10  |
| C $z$ -relaxation (10 <sup>-3</sup> Å)             | 194   | 18    | 72    | 118   | 145   | 182   | 442   |

See text for property definitions.

This surface atom position variance in Eq. (2), restricted to the direction normal to the surface, gives a quantitative measure of the surface roughness. We note that the majority, if not all, of the rms relaxation for each surface is due to these surface layers, as the atoms in the inner third of each slab remain in mostly bulklike positions. We also report in Table 6 the structural relaxation in the surface normal direction of the C atom closest to the surface (C  $z$ -relaxation) for each surface.

The surface ordering presented in Table 6 shows decreasing  $E_{\text{surf,rel}}$  and thus increasing surface sta-

bility from left to right. Of the cementite surfaces examined, we found the (100) and (011) surfaces to be the least stable, the (001) surface to be the most stable, and all others surfaces to have similar stability in between. These trends do not correlate with our preliminary assessment based on initial packing density and dangling bonds for the unrelaxed surfaces. On the other hand, the relative stabilities correspond somewhat to our estimate of the surface roughness; less rough surfaces like (110) and (001) tend to have lower  $E_{\text{surf}}$ , while rougher surfaces tend to have higher  $E_{\text{surf}}$ . One can visualize this trend in Fig. 5, which shows side

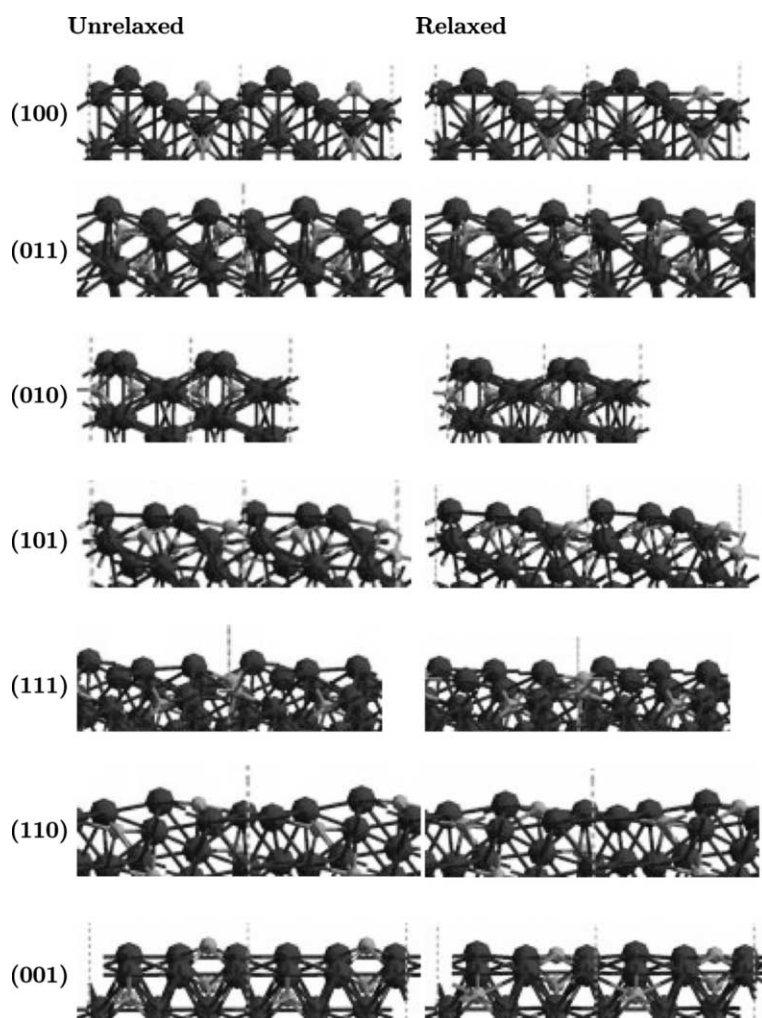


Fig. 5. Cross-sections of unrelaxed (left) and relaxed (right) cementite surface structures.

perspectives of each of the studied surfaces from highest  $E_{\text{surf}}$  (top) to lowest (bottom).

Overall, we see that bulk-terminated surfaces with higher surface energies ( $E_{\text{surf,unrel}}$ ) and higher roughness tend to have higher relaxation energies and greater rms position relaxation per unit surface area (Table 6). These trends are expected due to the greater potential for relaxation in less stable surfaces. However, the most stable surface, the (001) surface, is an exception, as it relaxes considerably in both atomic positions and surface energy, despite already possessing a relatively stable bulk-terminated structure. The special nature of the (001) surface is due to the behavior of the surface carbon, which relaxes dramatically further into the surface than carbons on other surfaces. The correlation of this large C  $z$ -relaxation with a similarly anomalously large relaxation energy suggests that the stability of the (001) surface originates with this carbon. For more insight into this result, we must explore other surface properties.

The local DOS of exposed-carbon cementite surfaces, like the (001) surface, changes dramatically when allowed to relax. Fig. 6 shows the site- and  $l$ -projected local DOS for the two most stable and two least stable cementite surfaces before and after relaxation. In all cases, the Fe  $d$  contribution to the DOS remains relatively unchanged upon structural relaxation. However, the change in the carbon  $s$  and  $p$  contributions to the DOS upon relaxation is noticeable, especially for the least [(100)] and most [(001)] stable surfaces. Examination of Fig. 5 reveals that both the (100) and (001) surfaces have highly exposed C atoms at their surfaces, while in all other surfaces the carbon atoms tend to be buried. In particular, the (110) surface has slightly less exposed C atoms, while the (011) surface is Fe-terminated, which correlates with the minimal change in the  $s$  and  $p$  DOS for these surfaces (Fig. 6). The significant shift in the C  $s$  and  $p$  states to lower energy (greater binding) for the (100) and (001) surfaces

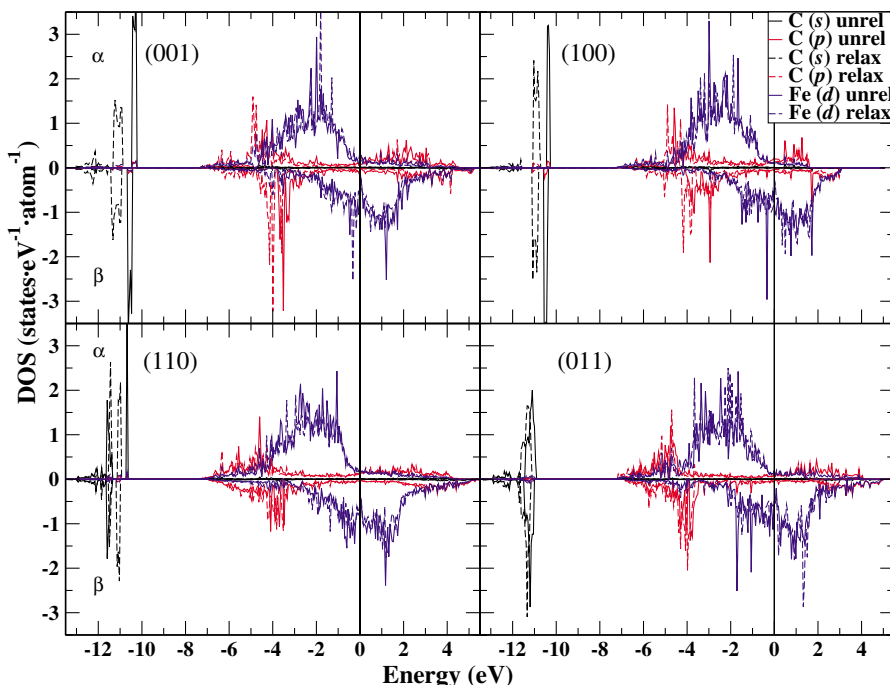


Fig. 6. DOS relaxation for the (001), (100), (110), and (011), surfaces of cementite. The plots show the DOS projected onto the atoms in the outer layer of a surface slab before (solid lines) and after (dashed lines) they are allowed to relax.  $\alpha$ -spin DOS are shown as positive;  $\beta$ -spin DOS are shown as negative.

correlates nicely with the observation that their surface C atoms move more than any other surface, moving toward the bulk in order to gain higher coordination. This higher coordination is rewarded by greater overlap in C p and Fe d states in the case of the (001) surface, suggesting a covalent contribution to the surface Fe–C interaction.

The geometric structures of the most and least stable surfaces have characteristics that determine the bonding of these surfaces. In particular, the average coordination numbers and bond distances differ significantly. For example, while the surface C atoms in both surfaces are five-coordinate, the surface Fe coordination differs. The least stable (100) surface has varied surface Fe coordination numbers (8–12). In contrast, each surface Fe in the most stable (001) surface has a coordination of exactly 9, akin to a face-centered cubic (111) surface. This coordination regularity correlates with a smoother, more uniform surface charge density distribution. Secondly, the average Fe–C distance at the surface decreases to 1.88 Å for the (001) surface, while the less stable (100) surface shows no such decrease compared to the bulk (2.00 Å). The decreased average Fe–C distances allow for a greater interaction between the surface C and adjacent Fe atoms on Fe<sub>3</sub>C (001). Fig. 7 provides evidence for these claims, via slices of the total valence charge density through the outermost surface atom, parallel to the surface. The (001) surface has a much more uniform density distribution in the slice plane than the (100) surface, which displays large gaps in density. We also see significant charge density localization between the Fe and C atoms at the (001) surface compared to little such Fe–C local bonding at the (100) surface. The decreased Fe–C distances on Fe<sub>3</sub>C (001) provide the optimal environment for localized Fe–C bonding. This localized Fe–C bonding is likely the origin of the (001) surface's extra stability.

Lastly, an important point of comparison for these predictions of cementite surface stabilities are the surface energies of bulk bcc iron. At the same level of theory (USPP-GGA), the pure Fe surfaces, (111), (100), and (110), have surface energies of 2.59, 2.30, and 2.29 J/m<sup>2</sup> [56], respectively. All but two of the cementite surfaces have lower predicted

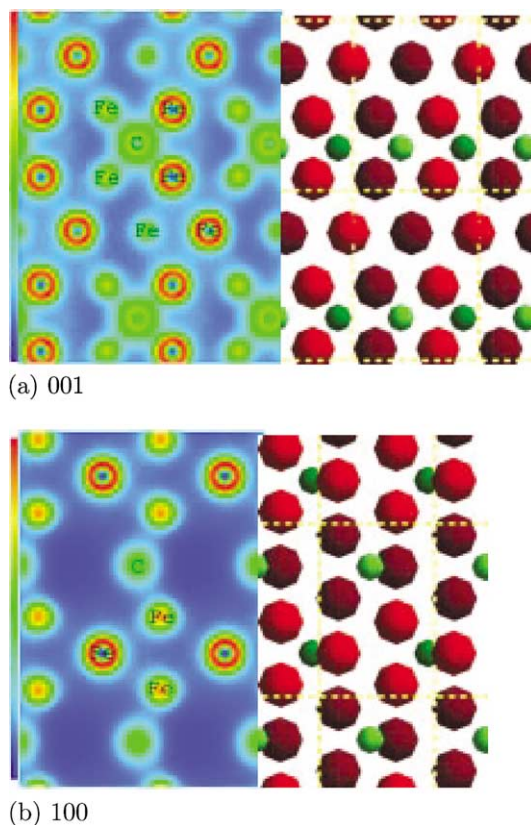


Fig. 7. Total valence charge densities of the most stable [(a), (001)] and least stable [(b), (100)] cementite surfaces on a logarithmic rainbow scale from blue (low density) to red (high density). The slices (parallel to the surface) are made through the outermost atom in each surface. To the right of each density plot is a schematic of the atoms in the top two layers, with Fe in red and C in green (the subsurface atoms are shaded darker).

surface energies than the most stable pure Fe surface. Importantly, the most stable cementite (001) surface has a 0.24 J/m<sup>2</sup> lower energy than the most stable bcc Fe (110) surface. Thus, formation of Fe<sub>3</sub>C surfaces may provide the driving force to carburize pure Fe, perhaps allowing Fe<sub>3</sub>C to form despite its known bulk metastability with respect to bcc Fe and graphite. We find, within USPP-GGA calculations at 0 K, bulk cementite to be more stable than bcc Fe and graphite by  $E_{\text{tot}}(\text{Fe}_3\text{C}, \text{ eV/atom}) - \frac{3}{4}E_{\text{tot}}(\text{bcc Fe}, \text{ eV/atom}) - \frac{1}{4}E_{\text{tot}}(\text{graphite}, \text{ eV/atom}) = -0.91 \text{ eV/atom}$ , where  $E_{\text{tot}}(\text{Fe}_3\text{C})$  in eV/atom is the total energy (in eV) of the 16-atom cementite unit cell divided by 16,

$E_{\text{tot}}(\text{bcc Fe})$  in eV/atom is the total energy of the one-atom bcc Fe unit cell, and  $E_{\text{tot}}(\text{graphite})$  in eV/atom is the total energy of the two-atom graphite unit cell divided by 2. Given the known metastability of bulk cementite, this may be an overestimate of its true stability.

#### 4. Summary

We have presented properties derived from spin-polarized USPP DFT-GGA calculations on  $\text{Fe}_3\text{C}$  in the cementite structure, in its bulk form and for its low-index surfaces. The GGA bulk properties agree quite well with the experimental lattice parameters and magnetic moments, while the bulk modulus differs significantly. Our cohesive energy (5.24 eV/atom) is quite close to an experimental estimate (5.05 eV/atom), lending confidence in the accuracy of our subsequent surface energy predictions. As expected, the bulk cementite DOS indicates mostly metallic behavior for  $\text{Fe}_3\text{C}$ , but the Fe–C interaction involves slight charge transfer from Fe to C, along with a significant Fe(d)–C(p) covalent component to the bonding.

Our cementite surface calculations predict the (001) surface to be the most stable and the (100) surface to be the least stable, with surface energies of 2.05 and 2.47 J/m<sup>2</sup> respectively. These two surfaces show the greatest relaxation energies, which correlates also with the largest change in position of their C atoms at the surface. In the case of the most stable surface, this relaxation is more than twice as large (in Å) as that for the least stable surface. Overall, the cementite relative stabilities correlate well with the rms roughness of the associated surface. The impact of the rougher configuration of the (100) surface is that it produces gaps in its charge density distribution in the outermost surface plane, reducing Fe–C bonding, leading to a less stable surface. By contrast, the smoother (001) surface produces a more uniform charge density across the surface plane, with *clear evidence of localized Fe–C bonding* that undoubtedly stabilizes this surface. A stable (001) surface is consistent with a previous report that cementite forms a  $[002]_{\text{cementite}}/[011]_{\text{Fe}}$  interface with iron [29].

Our results provide possible insight into the carburization erosion mechanism for steel. It takes 0.24 J/m<sup>2</sup> less energy to create the cementite (001) surface than the pure bcc-Fe (110) surface from their respective bulk crystals; thus, the surface thermodynamics favor carburization at Fe surfaces. In addition, if these surfaces are created and exposed during carburization, the cementite (001) surface may be more likely to erode due to cracking than the pure Fe (110) surface, ignoring plasticity effects excluded from our calculation. Even if the (001) cementite surface is not explicitly formed, cracking along several low-Miller-index directions in bulk cementite may be more likely than along either the (110), (100), or (111) directions in pure iron. Furthermore, given that surfaces tend to “pre-melt” at lower temperatures than the bulk melting point, and given that the melting point of cementite is far below that of bulk Fe, it is likely that these  $\text{Fe}_3\text{C}$  surfaces will pre-melt, providing the means for steel to erode. These conclusions do not contradict the findings of Wu et al. [31] that find carbon to increase the cohesion at Fe grain boundaries, but rather extend them. Low carbon concentration indeed increases the strength of bulk iron, as in commercial steels, but greater carbon concentration and the subsequent formation of cementite-phase iron carbide can have the opposite destructive effect.

Of course, these calculations are conducted in the presence of vacuum. Atmospheric contaminants, such as those present in true carburizing environments will undoubtedly alter the situation, perhaps producing surfaces with non-stoichiometric compositions not considered here. The bulk and surface properties of cementite predicted here are intended to serve as a starting point for larger-scale erosion modeling to examine more fully the steel carburization problem.

#### Acknowledgements

W.C. is grateful to Dr. Emily A.A. Jarvis for technical assistance and Dr. Ashok Arya for project discussions. This work is supported by the US Army Research Office, contract DAAD19-99-1-0227, and calculations were conducted at the Maui

## High Performance Computing Facility and the Army Research Laboratory Major Shared Resource Center.

### References

- [1] H.K. Grabke, *Carburization: A High Temperature Corrosion Phenomenon.*, MTI, St. Louis, 1998.
- [2] P.J. Cote, C. Rickard, *Wear* 241 (2000) 17.
- [3] D.M. Turley, *Wear* 131 (1989) 135.
- [4] I. Ahmad, The problem of gun barrel erosion—an overview, in: L. Stiefel (Ed.), *Gun Propulsion Technology*, AIAA, Washington, DC, 1988, pp. 311–355.
- [5] O. Botstein, R. Arone, *Wear* 142 (1991) 87.
- [6] J.S. Underwood, A.P. Parker, P.J. Cote, S. Sopok, *Trans. ASME* 121 (1999) 116.
- [7] P.J. Conroy, P. Weinacht, M.J. Nusca, An investigation of the erosion physics/mechanisms of current army systems (point studies), Army Research Laboratory ARL-TR-2054, September 1999.
- [8] E. Pippel, J. Woltersdorf, H.J. Grabke, S. Strauss, *Steel Res.* 66 (1995) 217.
- [9] E. Pippel, J. Woltersdorf, R. Schneider, *Mater. Corros.* 49 (1998) 309.
- [10] H.J. Grabke, *Mater. Corros.* 49 (1998) 303.
- [11] T.Y. Kosolapova, *Carbides: Properties, Production, and Applications*, Plenum, New York, 1971.
- [12] V. Raghavan, *Phase Diagrams of Ternary Iron Alloys*, ASM, Materials Park, 1987.
- [13] H. Lipson, N.J. Petch, *J. Iron Steel Inst.* 142 (1940) 95.
- [14] E.J. Fasiska, G.A. Jeffrey, *Acta Cryst.* 19 (1965) 463.
- [15] T. Hahn (Ed.), *International Tables for Crystallography*, Vol. A, Reidel, Dordrecht, 1983.
- [16] A.H. Cottrell, *Mat. Sci. Tech.* 9 (1993) 277.
- [17] A. Königer, C. Hammerl, M. Zeitler, B. Rauschenbach, *Phys. Rev. B* 55 (1997) 8143.
- [18] C. Hammerl, A. Königer, B. Rauschenbach, *J. Mater. Res.* 13 (1998) 2614.
- [19] W. Arabczyk, U. Narkiewicz, *Vacuum* 48 (1997) 347.
- [20] X.L. Dong, Z.D. Zhang, Q.F. Xiao, X.G. Zhao, Y.C. Chuang, S.R. Jin, W.M. Sun, Z.J. Li, Z.X. Zheng, H. Yang, *J. Mater. Sci.* 33 (1998) 1915.
- [21] X.Q. Zhao, Y. Liang, Z.Q. Hu, B.X. Liu, *J. Appl. Phys.* 80 (1996) 5857.
- [22] S.J. Li, M. Ishihara, H. Yumoto, T. Aizawa, M. Shimotomai, *Thin Solid Films* 316 (1998) 100.
- [23] H. Mizubayashi, S.J. Li, H. Yumoto, M. Shimotomai, *Scripta Mater.* 40 (1999) 773.
- [24] J. Li, H.K. Mao, Y. Fei, E. Gregoryanz, M. Erements, C.S. Zha, *Phys. Chem. Minerals* 29 (2002) 166.
- [25] R.C. Reed, J.H. Root, *Scripta Mater.* 38 (1998) 95.
- [26] I.N. Shabanova, V.A. Trapeznikov, *JETP Lett.* 18 (1973) 339.
- [27] I.N. Shabanova, V.A. Trapeznikov, *Pis'ma Zh. Eksp. Teor. Fiz.* 18 (1973) 576.
- [28] I.N. Shabanova, V.A. Trapeznikov, *Pis'ma Zh. Eksp. Teor. Fiz.* 6 (1975) 297.
- [29] K. Inokuti, *Tetsu to Hagane* 85 (1999) 628.
- [30] Y. Ohmori, Y.C. Jung, K. Nakai, H. Shioiri, *Acta Mater.* 49 (2001) 3149.
- [31] R. Wu, A.J. Freeman, G.B. Olson, *Phys. Rev. B* 53 (1996) 7504.
- [32] J. Häglund, G. Grimvall, T. Jarlborg, *Phys. Rev. B* 44 (1991) 2914.
- [33] A.G. Vakhnej, V.N. Antonov, A.N. Yaresco, V.V. Nemoshkalenko, V.G. Gavrilyuk, *Metallofiz. Nov. Tekh.* 18 (1996) 21.
- [34] P. Hohenberg, W. Kohn, *Phys. Rev. B* 136 (1964) 864.
- [35] W. Kohn, L.J. Sham, *Phys. Rev. A* 140 (1965) 1133.
- [36] G. Kresse, J. Hafner, *Phys. Rev. B* 47 (1993) 558.
- [37] G. Kresse, J. Hafner, *Phys. Rev. B* 49 (1994) 14251.
- [38] G. Kresse, J. Furthmüller, *Comput. Mater. Sci.* 6 (1996) 15.
- [39] D. Vanderbilt, *Phys. Rev. B* 41 (1990) 7892.
- [40] G. Kresse, J. Hafner, *J. Phys.: Condens. Matter* 6 (1994) 8245.
- [41] J.P. Perdew, in: P. Ziesche, H. Eschrig (Eds.), *Electronic Structure of Solids*, Akademie Verlag, Berlin, 1991, p. 11.
- [42] J.P. Perdew, J.A. Chevary, S.H. Vosko, K.A. Jackson, M.R. Pederson, D.J. Singh, C. Fiolhais, *Phys. Rev. B* 46 (1992) 6671.
- [43] P. Bagno, O. Jepsen, O. Gunnarsson, *Phys. Rev. B* 40 (1989) 1997.
- [44] E.G. Moroni, G. Kresse, J. Hafner, J. Furthmüller, *Phys. Rev. B* 56 (1997) 15629.
- [45] A.M. Rappe, K.M. Rabe, E. Kaxiras, J.D. Joannopoulos, *Phys. Rev. B* 41 (1990) 1227.
- [46] M. Methfessel, A.T. Paxton, *Phys. Rev. B* 40 (1989) 3616.
- [47] P.E. Blöchl, O. Jepsen, O.K. Andersen, *Phys. Rev. B* 49 (1994) 16223.
- [48] P. Pulay, *Chem. Phys. Lett.* 73 (1980) 393.
- [49] C.G. Broyden, *Math. Comput.* 19 (1965) 577.
- [50] D.D. Johnson, *Phys. Rev. B* 38 (1988) 120877.
- [51] D.M. Bylander, L. Kleinman, *Phys. Rev. B* 46 (1992) 9837.
- [52] J. Häglund, A.F. Guillermet, G. Grimvall, M. Körling, *Phys. Rev. B* 48 (1993) 11685.
- [53] G. Kresse, J. Furthmüller, *VASP the GUIDE*, Vienna, 1999. Available from <<http://cms.mpi.univie.ac.at/vasp/vasp.ps.Z>>.
- [54] F.D. Murnaghan, *Am. J. Math.* 49 (1937) 235.
- [55] F. Birch, *Phys. Rev.* 71 (1947) 809.
- [56] A. Arya, E.A. Carter, *J. Chem. Phys.*, in press.